parameter space where self-healing cracks were predicted to exist. Because of the long running times and complicated initial conditions needed to produce steady states, we have limited ourselves to small systems of about 500,000 atoms. We have found three self-healing cracks consistent with the analytical predictions; a picture of one of them appears in Fig. 1.

With the catalogue of self-healing cracks in hand, we now return to the matter of how they lead to friction. For any given compressive stress ($-\sigma_{yy}(\infty)$) there is a minimum shear stress $\sigma_{xy}(\infty) \approx -0.2\sigma_{yy}(\infty)$ that allows the cracks to begin moving (see Fig. 2a). For any smaller shear stress, the upper block cannot slide; for any larger shear stress, there is a way for it to slide. This sliding is well described by a coefficient of friction to the extent that the lower boundary of states can be approximated by a straight line. The lower boundary of states depends only weakly upon the model parameters, which include bond stiffness and interface strength.

What we have in fact determined is a lower bound on a coefficient of static friction at zero temperature. Static friction will be determined by when self-healing cracks actually initiate, which is not necessarily identical with when they first become possible. Once sliding begins, properties of kinetic friction will be determined by populations of self-healing cracks. The speed at which the upper block slides will depend upon the number of self-healing cracks moving at any time, and is not directly determined by the speeds of these cracks.

The question of when self-healing cracks actually underlie frictional sliding will have to be settled by experiments. There is some evidence for such cracks from experiments aimed at settling questions about earthquakes[5–7]. Real surfaces are certainly not flat enough over macroscopic lengths for our description of friction to be complete, and other mechanisms of frictional sliding[1,24] will certainly compete with this one. However, we believe that our calculation of a friction coefficient from the atomic scale up constitutes progress. We hope that these definite mathematical results for an ideal case will be useful for proceeding to more realistic ones, and will motivate new experiments. □

Received 7 March; accepted 11 August 2001.

1. Persson, B. N. J. *Sliding Friction: Physical Principles and Applications* (Springer, Heidelberg, 1998).
2. Comninou, M. & Dundurs, J. Can solids slide without slipping? *Int. J. Solids Struct.* **14,** 251–260 (1978).
3. Weertman, J. Unstable slippage across a fault that separates elastic media of different elastic constants. *J. Geophys. Res. B* **85,** 1455–1461 (1980).
4. Caroli, C. Slip pulses at a sheared frictional viscoelastic/nondeformable interface. *Phys. Rev. E* **62,** 1729–1735 (2000).
5. Brune, J. N., Brown, S. & Johnson, P. A. Rupture mechanism and interface separation in foam rubber models of earthquakes: a possible solution to the heat flow paradox and the paradox of large overthrust. *Tectonophysics* **218,** 59–67 (1993).
6. Brown, S. R. Frictional heating on faults: Stable sliding versus stick slip. *J. Geophys. Res.* **103,** 7413–7420 (1998).
7. Anooshehpoor, A. & Brune, J. N. Wrinkle-like Weertman pulse at the interface between two blocks of foam rubber with different velocities. *Geophys. Res. Lett.* **26,** 2025–2028 (1999).
8. Scott, R. S. Seismicity and stress rotation in a granular model of the brittle crust. *Nature* **381,** 5922–595 (1996).
9. Ben-Zion, Y. & Andrews, D. J. Properties and implications of dynamic rupture along a material interface. *Bull. Seismol. Soc. Am.* **88,** 1085–1094 (1998).
10. Mora, P. The weakness of earthquake faults. *Geophys. Res. Lett.* **26,** 123–126 (1999).
11. Place, D. & Mora, P. The lattice solid model to simulate the physics of rocks and earthquakes: incorporation of friction. *J. Comput. Phys.* **150,** 332–372 (1999).
12. Freund, L. B. *Dynamic Fracture Mechanics* (Cambridge Univ. Press, Cambridge, 1990).
13. Dhaliwal, R. J. & Saxena, H. S. Moving Griffith crack at the interface of two orthotropic elastic layers. *J. Math. Phys. Sci.* **26,** 237–254 (1992).
14. Das, S. & Patra, B. Moving Griffith crack at the interface of two dissimilar orthotropic half planes. *Eng. Fract. Mech.* **54,** 523–531 (1996).
15. Ranjith, K. & Rice, J. R. Slip dynamics at an interface between dissimilar materials. *J. Mech. Phys. Solids* **49,** 341–361 (2001).
16. Cochard, A. & Rice, J. R. Fault rupture between dissimilar materials: III-posedness, regularization, and slip-pulse response. *J. Geophys. Res. B* **105,** 25891–25907 (2001).
17. Slepyan, L. I. Plane problem of a crack in a lattice. *Izv. Akad. Nauk SSSR Mekh. Tverd. Tela* **16,** 101–115 (1982).
18. Marder, M. & Gross, S. Origin of crack tip instabilities. *J. Mech. Phys. Solids* **43,** 1–48 (1995).
19. Wilson, G. T. The factorization of matrixial spectral densities. *SIAM J. Appl. Math.* **23,** 420–426 (1972).
20. Eggermont, P. & Lubich, C. Fast numerical solution of singular integral equations. *J. Integral Equations Appl.* **6,** 335–351 (1994).
21. Williams, M. L. The stresses around a fault or crack in dissimilar media. *Bull. Seismol. Soc. Am.* **49,** 199–204 (1959).
22. Deng, X. Complete complex series expansions of near-tip fields for steadily growing interface cracks in dissimilar isotropic materials. *Eng. Fract. Mech.* **42,** 237–242 (1992).
23. Holland, D. & Marder, M. Cracks and atoms. *Adv. Mater.* **11,** 793–806 (1999).
24. Müser, M. H., Wenning, L. & Robbins, M. O. Simple microscopic theory of Amontons's laws for static friction. *Phys. Rev. Lett.* **86,** 1295–1298 (2001).
25. Heaton, T. H. Evidence for and implications of self-healing pulses of slip in earthquake rupture. *Phys. Earth Planet. Interiors* **64,** 1–20 (1990).
26. Adams, G. G. Dyanmic motion of two elastic half-spaces in relative sliding without slipping. *J. Tribol.* **121,** 455–461 (1999).
27. Ranjith, K. & Rice, J. R. Slip dynamics at an interface between dissimilar materials. *J. Mech. Phys. Solids* **49,** 341–361 (2001).

Acknowledgements

We thank H. Swinney for suggestions on presentation. This work was supported by the NSF and by a fellowship from TICAM at The University of Texas at Austin.

Correspondence and requests for materials should be addressed to M.M. (e-mail: marder@chaos.ph.utexas.edu).

A high-strain-rate superplastic ceramic

B.-N. Kim, K. Hiraga, K. Morita & Y. Sakka

National Institute for Materials Science, 1-2-1 Sengen, Tsukuba, Ibaraki 305-0047, Japan

High-strain-rate superplasticity describes the ability of a material to sustain large plastic deformation in tension at high strain rates of the order of 10^{-2} to 10^{-1} s^{-1} and is of great technological interest for the shape-forming of engineering materials. High-strain-rate superplasticity has been observed in aluminium-based[1] and magnesium-based[2] alloys. But for ceramic materials, superplastic deformation has been restricted to low strain rates of the order of 10^{-5} to 10^{-4} s^{-1} for most oxides[3,4] and nitrides[5] with the presence of intergranular cavities leading to premature failure. Here we show that a composite ceramic material consisting of tetragonal zirconium oxide, magnesium aluminate spinel and α-alumina phases exhibits superplasticity at strain rates up to 1 s^{-1}. The composite also exhibits a large tensile elongation, exceeding 1,050 per cent for a strain rate of 0.4 s^{-1}. The tensile flow behaviour and deformed microstructure of the material indicate that superplasticity is due to a combination of limited grain growth in the constitutive phases and the intervention of dislocation-induced plasticity in the zirconium oxide phase. We suggest that the present results hold promise for the application of shape-forming technologies to ceramic materials.

In superplastic materials, the primary deformation mechanism is grain-boundary sliding, and it is the rate of this process that determines the macroscopic strain rate. Because cavitation due to grain-boundary sliding must be accommodated by diffusion and/or dislocation processes for successive deformation, a short accommodation length—which means a small grain size—is indispensable for attaining high-strain-rate superplasticity. For the same reason, stability of the small grain size is also essential. If grain growth occurs actively during deformation, the accommodation length increases and retards facile grain-boundary sliding. This causes an increase in the level of stress necessary for successive deformation—that is, strain-hardening. Strain-hardening enhances the extent of stress concentration on the sliding grain boundaries or grain corners, resulting in the formation of intergranular cavities that leads to premature failure. We have fabricated a multi-phase

ceramic composite consisting of 40 vol.% ZrO_2, 30 vol.% spinel and 30 vol.% Al_2O_3; this material has submicrometre-sized grains and grain growth is strongly suppressed by dispersed phases.

The starting materials were commercial powders of high purity α-Al_2O_3 (>99.99%, TM-DAR, Taimei Chemical), tetragonal ZrO_2 stabilized by 3 mol% Y_2O_3 (>99.97%, TZ-3Y, Tosoh) and MgO (>99.97%, 100A, Ube Chemical) with nominal particle diameters of 0.2, 0.07 and 0.017 μm, respectively. The powders were mixed in a ball-mill, using balls of pure Al_2O_3 (>99.9%) and ethanol. After drying and granulation with a 60-mesh sieve, the mixed powder was pressed at 40 MPa and then cold-isostatically pressed at 200 MPa. The compacts were sintered at 1,400 °C for 1 h in air, during which a spinel phase was formed by chemical reaction between the MgO and Al_2O_3 powders. The density of the sintered body was 4.57 g cm^{-3}. As shown in Fig. 1, the sintered microstructure consisted of equiaxed α-Al_2O_3, spinel and tetragonal ZrO_2 grains. The average grain size, defined as the equivalent area diameter of the grain measured by scanning electron micrography (SEM), was 0.29 μm for the Al_2O_3 phase, and 0.18 μm for both ZrO_2 and spinel phases. The mean grain size of these phases was 0.21 μm.

From the sintered compacts, flat tensile specimens were machined with a gauge length of 8 mm, a width of 3 mm and a thickness of 2 mm. Constant-displacement-rate tensile tests were performed with an Instron-type testing machine at 1,650 °C in vacuum. Tensile strain and stress were determined from the cross-head displacement by considering the compliance of the testing machine and by assuming uniform elongation in the gauge portion. At the test temperature, the grain sizes just before deformation were about twice the as-sintered ones.

As shown in Fig. 2, tensile deformation in the present material proceeded uniformly without local necking, and tensile elongation reached 390% at an initial strain rate of 1 s^{-1}. To our knowledge, this is the highest strain rate reported for any superplastic ceramic material. At a slightly lower strain rate of 0.4 s^{-1}, the material did not fail even after the tensile elongation reached 1,050%, which is the maximum elongation that can be examined with the present testing machine. An elongation to failure of 1,040%, which is (to our knowledge) the maximum value so far recorded in ceramics, has been attained in a Y_2O_3-stabilized tetragonal ZrO_2 doped with 5 wt% (~13 vol.%) SiO_2 at an initial strain rate of 1.3×10^{-4} s^{-1}

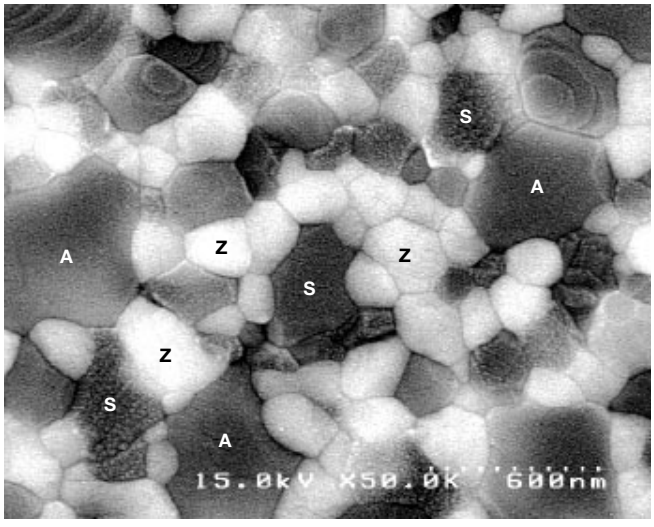

Figure 1 Scanning electron micrograph of the as-sintered microstructure. Grain labels A, S and Z represent Al_2O_3, spinel and ZrO_2, respectively. The constitutive phases were identified by X-ray diffraction. The molar Al_2O_3 to MgO ratio in the spinel phase was also determined by X-ray diffraction as 1.1 for the as-sintered material and 2.2 for a specimen quenched from the deformation temperature.

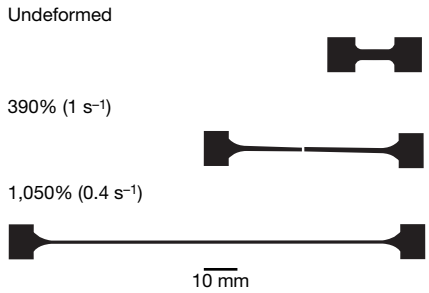

Figure 2 Specimens before and after deformation at 1,650 °C. At 0.4 s^{-1}, the tensile test was terminated before failure owing to a limitation of the loading span available in the testing machine.

(ref. 4). It should be noted, however, that the strain rate to attain the 1,050% elongation in the present material is more than 3,000 times higher than that available for the SiO_2-doped material. We also note that such a difference in the available strain rate leads to quite a large difference in the deformation time: to attain an elongation of 1,000%, for example, it takes 20 h at 1.3×10^{-4} s^{-1} in the SiO_2-doped ZrO_2, whereas it takes only 25 s at 0.4 s^{-1} in the present material.

Tensile flow data (Fig. 3) exhibit some characteristics different from those of other superplastic ceramics[1,3–5]. The first point is the lack of strain-hardening in the present material. Flow stress either starts to decrease immediately after yielding (1 s^{-1}), or it remains almost constant up to a tensile strain of 0.8 and then gradually decreases (0.4 s^{-1}). This is in contrast to the general behaviour of other superplastic ceramics, where strain-hardening occurs through grain growth, and is followed by a decrease in flow stress; this decrease is mainly due to a decrease in strain rate with increasing strain under constant-displacement-rate loading, and partially to cavitation at large strains. Microstructural examination of the deformed specimens revealed that the lack of strain-hardening is due mainly to highly limited grain growth. The increment of grain size in each phase was about 10% or less after deformation to failure.

There are two possible explanations for the limited grain growth in the present material; the heightened strain rates and the particle dispersion. The extent of grain growth is proportional to the deformation time and strain[6]. Hence, the shorter the deformation time or the smaller the tensile strain, the smaller the increment of

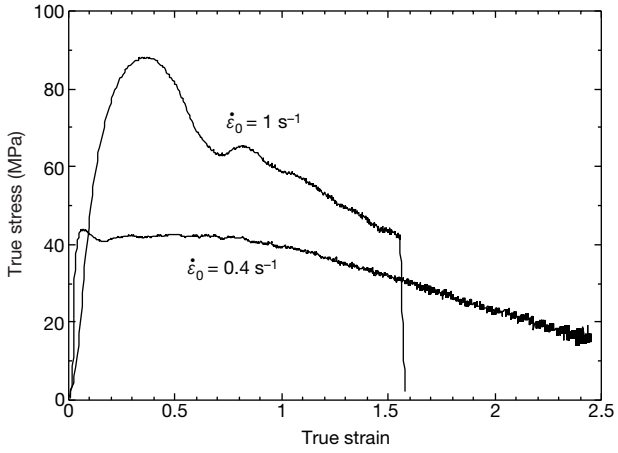

Figure 3 Stress–strain curves at 1,650 °C. $\dot{\epsilon}_0$ is the initial strain rate. We note that the undulated feature after yielding, particularly at $\dot{\epsilon}_0 = 1\,s^{-1}$, is typical of dynamic recrystallization in metallic materials. The extent of yield-drop increases with increasing strain rate.

grain size—and in our material there is a shortened deformation time due to the heightened strain rates. As far as particle dispersion is concerned, the present material has characteristics different from those of conventional materials: a tri-phase structure, where the amount of each phase is similar. For a given volume of dispersed particles, such a tri-phase structure decreases the frequency of the grain boundaries between the same phases or increases the separation distance between the phases. This situation is of benefit to the suppression of grain growth, as grain growth occurs by the migration of such grain boundaries and/or by the coarsening of grains through interphase boundary diffusion. For the same reason, an increase in the amount of dispersed particles is known to enhance the suppression of grain growth[7]. Indeed, the mean grain size of 0.21 μm in the present 30 vol.% Al_2O_3–40 vol.% ZrO_2–30 vol.% spinel is much smaller than that of 80 vol.% Al_2O_3–10 vol.% ZrO_2–10 vol.% spinel[8], where the mean grain size reached 0.45 μm for a similar sintering procedure. Thus, the limited grain growth in the present material can be attributed to both the heightened strain rates and the multi-phase structure.

Another point to note in the data shown in Fig. 3 is the yield-drop appearing just after initial yielding, accompanied by an indication of undulated flow. The yield-drop becomes more prominent with increasing strain rate. Such flow behaviour is known to appear during high-temperature plastic deformation in metallic polycrystals and single crystals owing to dislocation processes including dynamic recrystallization[9], but not in superplastic (or superplastic-like) polycrystalline ceramics. This non-appearance can be rationalized by the generally accepted considerations that grains in superplastic ceramics behave as rigid bodies and deformation occurs through grain-boundary sliding accommodated by diffusion[1,3–5]. Thus, the flow behaviour shown in Fig. 3 suggests that other deformation mechanisms may intervene in the high-strain-rate deformation of the present material.

Figure 4 shows a typical example of substructures developed in ZrO_2 grains during high-strain-rate deformation. Dense intergranular dislocations, some of which are tangled, and the occurrence of subgrain boundaries are characteristics of the ZrO_2 grains after deformation. This observation indicates that dislocations were generated and moved in the ZrO_2 grains during deformation. In other words, the ZrO_2 grains are not rigid, but are deformed plastically to some extent during the high-strain-rate deformation.

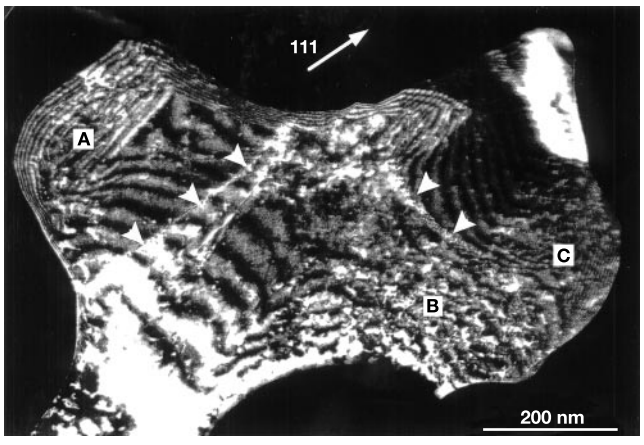

Figure 4 Transmission electron micrograph of a ZrO_2 grain in a specimen deformed to an elongation of 390% at 1,650 °C and at an initial strain rate of 1 s^{-1}. Dislocation substructures developed during high-strain-rate deformation can be seen. Intergranular dislocations, some of which are tangled, are seen around positions A, B and C. White arrow-heads indicate subgrain boundaries. These substructures do not appear in undeformed specimens.

Such dislocation activity has also been found recently in some fine-grained oxides such as spinel[10] and tetragonal ZrO_2 (ref. 11). The observation also indicates that the dislocations were rearranged to form subgrain boundaries during deformation—that is, dynamic recovery occurred in the ZrO_2 grains. The observed features imply that the ZrO_2 grains may contribute to the accommodation process of grain-boundary sliding through their plasticity. This means equivalently that the stress concentration developed during deformation can be relaxed not only by diffusion processes, but also by the plasticity of the ZrO_2 grains. Such a consideration is supported by the following cavitation behaviour in this material.

Cavitation damage in the present material was found to be quite limited during high-strain-rate tensile deformation. Although cavity stringers along the stress axis occurred at large strains, microcracks along the direction normal to the stress axis, which are often found in existing superplastic ceramics[12], were not observed. The average cavity volume fraction measured along the gauge portion was 0.051 and 0.061 for the specimens deformed at 1 s^{-1} (failed at 390% elongation) and 0.4 s^{-1} (elongated to 1,050%), respectively. At 0.1 s^{-1}, the cavity volume fraction was less than 0.025 at an elongation of about 1,000%. These values are quite small compared to those of other superplastic ceramics: in a Y_2O_3-stabilized tetragonal ZrO_2, which is a representative superplastic ceramic material, the cavity volume fraction reached 0.3 at an elongation of 700% at 1,550 °C and at a strain rate of 8.3×10^{-5} s^{-1} (ref. 12). At smaller tensile strains of around 100%, where most actual plastic forming has been performed in metallic materials, the level of cavitation damage can be further suppressed in this material. At a strain rate of 0.4 s^{-1}, for example, the cavity volume fraction after 100% elongation was evaluated to be less than 0.005 from the interpolation of the obtained data, and this value is similar to that which occurs in metal forming[13].

The suppression of cavity formation, which enables the large elongation in the present material, indicates that stress concentrations generated at grain boundaries and corners are sufficiently relaxed during deformation—if the stress relaxation was insufficient, cavitation would be much enhanced. In conventional superplastic ceramics, the relaxation occurs through diffusion[14], and we expect that this is also the case in the present material. However, the differences in cavitation behaviour and available strain rates between the conventional and the present materials indicate that an additional mechanism is at work in the latter. We attribute the occurrence of the additional relaxation to the above-mentioned dislocation-induced plasticity of the ZrO_2 dispersed among the other constitutive grains.

We thus conclude that the attainment of high-strain-rate superplasticity and the large tensile elongation in the present ZrO_2–spinel–Al_2O_3 composite arises from the multi-phase structure. This structure enables the achievement of submicrometre-sized grain structure after sintering and strongly suppressed grain growth during deformation. Furthermore, the dislocation-induced plasticity in the ZrO_2 grains is likely to play an additional role in the accommodation of grain-boundary sliding, that is, stress relaxation during high-strain-rate deformation.

The present results show that it is possible to overcome the major drawbacks of conventional superplastic ceramics in engineering applications, namely the low strain rate available for forming[15] and the extensive cavitation. We accordingly consider that, although problems remain to be solved in the area of further suppressing cavitation damage during deformation, the present results provide a way of applying superplasticity to the shape-forming of ceramic materials. □

Received 31 January; accepted 18 July 2001.

1. Nieh, T. G., Gilman, P. S. & Wadsworth, J. Extended ductility at high strain rates in a mechanically alloyed aluminum alloy. *Scripta Metall.* **19,** 1375–1378 (1985).
2. Mabuchi, M. & Higashi, K. High-strain-rate superplasticity in magnesium matrix composites containing Mg_2Si particles. *Phil. Mag. A* **74,** 887–905 (1996).

3. Wakai, F., Sakaguchi, S. & Matsuno, Y. Superplasticity of yttria-stabilized tetragonal ZrO_2 polycrystals. *Adv. Ceram. Mater.* **1,** 259–263 (1986).
4. Kajihara, K., Yoshizawa, Y. & Sakuma, T. The enhancement of superplastic flow in tetragonal zirconia polycrystals with SiO_2-doping. *Acta Metall. Mater.* **43,** 1235–1242 (1995).
5. Wakai, F. *et al.* A superplastic covalent crystal composite. *Nature* **344,** 421–423 (1990).
6. Kim, B.-N., Hiraga, K., Sakka, Y. & Ahn, B.-W. A grain boundary diffusion model of dynamic grain growth during superplastic deformation. *Acta Mater.* **47,** 3433–3439 (1999).
7. Smith, C. S. Grains, phases and interfaces: an interpretation of microstructure. *Trans. Metall. Soc. AIME* **175,** 15–51 (1948).
8. Kim, B.-N., Hiraga, K., Morita, K. & Sakka, Y. Superplasticity in alumina enhanced by co-dispersion of 10% zirconia and 10% spinel particles. *Acta Mater.* **49,** 887–895 (2001).
9. McQueen, H. J. & Jonas, J. J. in *Treatise on Materials Science and Technology* Vol. 6 (ed. Arsenault, R. J.) 393–493 (Academic, New York, 1975).
10. Ting, C.-J. & Lu, H.-Y. Hot-pressing of magnesium aluminate spinel—II. microstructure development. *Acta Mater.* **47,** 831–840 (1999).
11. Morita, K. & Hiraga, K. Deformed substructures in fine-grained tetragonal zirconia. *Phil. Mag. Lett.* **81,** 311–319 (2001).
12. Schissler, D. J., Chokshi, A. H., Nieh, T. G. & Wadworth, J. Microstructural aspects of superplastic tensile deformation and cavitation failure in a fine-grained yttria stabilized tetragnal zirconia. *Acta Metall. Mater.* **39,** 3227–3236 (1991).
13. Pilling, J. & Ridley, N. Effect of hydrostatic pressure on cavitation in superplastic aluminium alloys. *Acta Mater.* **34,** 669–679 (1986).
14. Evans, A. G., Rice, J. R. & Hirth, J. P. Suppression of cavity formation in ceramics: prospects for superplasticity. *J. Am. Ceram. Soc.* **63,** 368–375 (1980).
15. Wittenauer, J. Applications of ceramic superplasticity: challenges and opportunities. *Mater. Sci. Forum* **243–245,** 653–662 (1997).

Acknowledgements

We thank N. Sekine for experimental assistance.

Correspondence and requests for materials should be addressed to B.N.K. (e-mail: KIM.Byung-Nam@nims.go.jp).

Ultrafast holographic nanopatterning of biocatalytically formed silica

Lawrence L. Brott*, Rajesh R. Naik*, David J. Pikas*, Sean M. Kirkpatrick*, David W. Tomlin*, Patrick W. Whitlock*†, Stephen J. Clarson† & Morley O. Stone*

* *Materials and Manufacturing Directorate, Air Force Research Laboratory, 3005 P Street, Wright-Patterson Air Force Base, Ohio 45433-7702, USA*
† *Department of Materials Science and Engineering, University of Cincinnati, 497 Rhodes Hall, Cincinnati, Ohio 45221-0012, USA*

Diatoms are of interest to the materials research community because of their ability to create highly complex and intricate silica structures under physiological conditions: what these single-cell organisms accomplish so elegantly in nature requires extreme laboratory conditions to duplicate[1,2]—this is true for even the simplest of structures. Following the identification of polycationic peptides from the diatom *Cylindrotheca fusiformis*, simple silica nanospheres can now be synthesized *in vitro* from silanes at nearly neutral pH and at ambient temperatures and pressures[3,4]. Here we describe a method for creating a hybrid organic/inorganic ordered nanostructure of silica spheres through the incorporation of a polycationic peptide (derived from the *C. fusiformis* silaffin-1 protein) into a polymer hologram created by two-photon-induced photopolymerization. When these peptide nanopatterned holographic structures are exposed to a silicic acid, an ordered array of silica nanospheres is deposited onto the clear polymer substrate. These structures exhibit a nearly fifty-fold increase in diffraction efficiency over a comparable polymer hologram without silica. This approach, combining the ease of processability of an organic polymer with the improved mechanical and optical properties of an inorganic material, could be of practical use for the fabrication of photonic devices.

We have recently developed a holographic two-photon-induced photopolymerization (H-TPIP) process[5] and here we describe how this technique can be used to prepare nanopatterned structures that contain biological macromolecules. Unlike conventional holograms formed through the use of ultraviolet lasers, holograms created through the two-photon process use an ultrafast infrared laser. Because infrared wavelengths typically do not alter the functionality of biological compounds, monomer formulations containing peptides can be polymerized without affecting the biological activity. We incorporated a peptide that has recently been shown to be responsible for biosilification into a formulation to be cured by a holographic two-photon-induced photopolymerization with the expectation that the peptide would be segregated into regions of low crosslinking density. The approach of using ultraviolet lasers to phase separate small liquid crystal molecules in a polymer-based hologram has been used extensively[6] and we hypothesized that this technique would also be applicable to the H-TPIP process. We predicted that exposing the peptide-containing structure to a liquid silane would cause silica to form in the holographic nanopattern (see Fig. 1) and that this hybrid organic/inorganic device would have a higher degree of order leading to a superior device compared to randomly ordered monolayers of silica on indium-tin oxide (ITO) coated glass[7].

A short 19-amino-acid R5 peptide unit (SSKKSGSYSGSKGSKRRIL) of the silaffin-1 precursor polypeptide from *C. fusiformis* is able to catalyse the formation of silica nanospheres within minutes when added to silicic acid at neutral pH and ambient temperature[3]. A chemically synthesized R5 peptide that lacks a post-translational modification of its lysine residues was used in the present work. The post-translational modification of lysine residues is required for silica formation under acidic pH conditions[3,8]. However, because our research was conducted under slightly basic conditions, the modification of the lysine residues was unnecessary. Consequently, work began by incorporating this peptide (0.80 mg in 16 μl of water) into a monomer formulation. This formulation consisted of 160 μl SR-9035, 0.022 g SR-399 (SR-9035 is a trimethylolpropane triacrylate and SR-399 is a dipentaerythritol pentaacrylate obtained from Sartomer which were used without the removal of inhibitor), 0.006 g triethanol amine and 0.005 g isopropyl thioxanthone; the entire mixture was heated for 15 min at 50 °C to aid in dissolution. The triacrylate was chosen for its high water miscibility which is due to its numerous ethylene glycol units, and the pentaacrylate was used to create a highly crosslinked system. The triethanol amine functions as a coinitiator and thioxanthone as the initiator. Typically, in a two-photon-initiated polymerization, a fluorescent chromophore is also required to absorb two photons of near-infrared laser light. The excited chromophore transfers its energy to the initiator which begins the polymerization process. However, we have found that the thioxanthone used in this formulation does not require highly coloured chromophores, and consequently, extremely large curing depths and exceptionally clear and colourless polymers are produced[9,10].

A thin layer (175 μm) of the monomer/peptide formulation was deposited onto a clean glass slide which was then placed in a miniature atmospheric chamber fitted with glass windows and

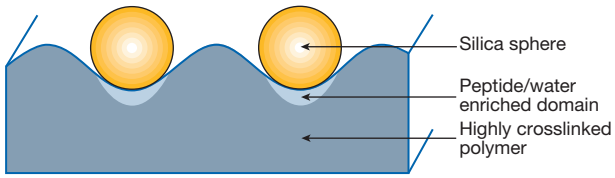

Figure 1 Cross-section of the hologram. The peptide-rich regions that are formed during the holographic polymerization process are shown.